OPEN

Fast Quantitative Low-Field Magnetic Resonance Imaging With OPTIMUM—Optimized Magnetic Resonance Fingerprinting Using a Stationary Steady-State Cartesian Approach and Accelerated Acquisition Schedules

Mathieu Sarracanie, PhD

Objective: The aim of the proposed work is to develop model-based, fast multiparametric magnetic resonance imaging (MRI) in field regimes where signal-to-noise ratio is poor, such as encountered at low-field and in low γ nuclei.

Materials and Methods: A custom, optimized MRI pipeline was developed at low field (0.1 T) that relies on the magnetic resonance fingerprinting framework, called OPTIMUM. An optimization algorithm was used to select a short acquisition schedule (n = 18 images) that favors maximal discrimination across varying magnetic properties (T_1, T_2) and off-resonance effects while maintaining high transverse magnetization at the steady state. In the presented study, a stationary balanced steady-state approach was investigated that allows for Cartesian (used here) and non-Cartesian acquisition schemes. Images were collected in calibrated samples containing different concentrations of manganese(II) chloride ($MnCl_2$) in deionized water and compared with gold standard techniques (ie, inversion recovery for T_1, Carr-Purcell-Meiboom-Gill for T_2). Images were then collected in vivo in the human hand and wrist.

Results: OPTIMUM successfully provided sets of quantified maps (T_1, T_2, T_2*, M_0, ΔB_0, B_1^+) in calibrated samples and in vivo in the human hand and wrist in 3 dimensions, in ~8.5 minutes, with a voxel resolution of [1.5 ×1.5 × 6.5] mm^3. Relaxation parameters (T_1, T_2) scale linearly with [$MnCl_2$] and are in good agreement with the calibrations performed for T_1, with a consistent trend to underestimate T_2.

Conclusion: We show that low-field MRI can benefit from innovative multiparametric approaches to gain speed and become realistic in clinical environments. For the first time, we report simultaneous, multiparametric imaging (6 quantitative maps) in 3 dimensions, in vivo in the human hand and wrist, obtained in just 8.5 minutes. It is sometimes overlooked that low magnetic fields provide higher dispersion of nuclear spin relaxation rates. Rapid quantification such as offered by OPTIMUM could be an enabling technology to explore new metrics and contrasts in point-of-care MRI diagnosis, making it an important step toward broad democratization.

Key Words: low-field MRI, multi-parametric imaging, MR fingerprinting

(*Invest Radiol* 2022;57: 263–271)

Received for publication July 21, 2021; and accepted for publication, after revision, September 7, 2021.

From the Center for Adaptable MRI Technology (AMT Center), Department of Biomedical Engineering, University of Basel, Allschwil, Switzerland.

Conflicts of interest and sources of funding: Swiss National Science Foundation (grant 186861).

Correspondence to: Mathieu Sarracanie, PhD, AMT Center, Department of Biomedical Engineering, University of Basel, Gewerbestrasse 14, 4123 Allschwil, Switzerland. E-mail: mathieu.sarracanie@unibas.ch.

ISSN: 0020-9996/22/5704–0263
DOI: 10.1097/RLI.0000000000000836

Magnetic resonance imaging (MRI) in radiology has steadily moved toward stronger magnetic fields to provide finer image resolution of body parts and function within the minimum acquisition time. This technical approach prioritizes sensitivity gain from increased nuclear polarization over weight, power requirements, or siting infrastructure considerations. Consequently, MRI scanners in radiology suites offer high performance but stay confined in a highly controlled environment that translates in tremendous costs and little (or no) flexibility. The prospect of agile MRI technology could be relevant in many areas though, from interventional settings to intensive care units where patients at risk need ongoing MRI monitoring.

The MRI community currently observes a resurgence of interest for low field (LF) that could enable such a paradigm change[1–5] and whose potential clinical value spans a very broad range whether on the upper (>0.2 T) or lower (<0.2 T) bound of the spectrum. If promising, such technologies face continuous challenges to reach clinical value that may trigger mass adoption. The intrinsically lower signal-to-noise ratio (SNR) per unit time calls for efficient acquisition schemes, supported by original reconstruction and processing pipelines, and innovative hardware solutions.

Often overlooked, nuclear relaxation mechanisms (longitudinal, T_1, and transverse, T_2 and T_2*) also play a major role in LF, with potential to unveil a diversity of clinically relevant, new endogenous contrasts. Largely unexplored, T_1 relaxation is known to exhibit higher dispersion at LF, as could be observed in the brain tissue,[6] whereas prolonged T_2 and T_2* inherently offer larger dynamic ranges. Unfortunately, spatial quantification of relaxation properties is generally unused at clinical fields (1.5–3 T) because of the additional acquisition time implied, and it is even harder to envision at LF to very-LF regimes. Indeed, T_1 and T_2 characterization relies on the calculation of time constants in the form of exponential decay/recovery curves, whose sampling strategy is adapted to the type of tissue or material investigated. In numerous applications, it is required to cover broad ranges of time constants that can result in prohibitive acquisition times. Hence, a general lack of quantitative data is commonly observed in clinical practice.

Promising methods exist that allow quickly probing of multiple properties of matter at once,[7–10] but rarely provide simultaneous quantification of an extensive range of typical MRI parameters such as T_1, T_2, T_2*, ΔB_0, or the transmit bias field B_1^+. Magnetic resonance fingerprinting (MRF),[11] introduced in 2013, is a model-based approach of MRI providing a set of quantitative nuclear magnetic resonance (NMR) maps at once, from a single magnetic resonance (MR) acquisition. Magnetic resonance fingerprinting consists of transient state sequences where a series of highly undersampled images are successively acquired while varying imaging parameters flip angle (FA) and repetition time (TR) simultaneously. Multiparametric maps are obtained by matching the acquired, time-varying signal pixelwise to a precomputed database of simulated MR signals. Since its introduction, MRF has gained considerable interest, and there have been many developments to improve it robustness, reliability, and expand its use.

Considering LF MRI, MRF transformed to fit this particular regime (ie, high T_1 dispersion, Johnson noise dominated) and constraints

(ie, low SNR, inhomogeneous fields, limited hardware performance) could make quantitative imaging clinically relevant. The MRF pipeline currently relies (most commonly) on hundreds[12,13] to thousands[11] of time-varying images acquired with a single-shot, highly undersampled spiral sampling of *k*-space (ie, non-Cartesian) following an inversion pulse. In multishot acquisitions, a delay is generally added at the end of each time series to allow for magnetization recovery. Such peculiarities make MRF a challenge to deploy at LF, in particular, on the lower end of the LF spectrum. Besides, single-shot spiral imaging is nontrivial to implement on non-commercial research LF systems; multishot (Cartesian or non-Cartesian) alternatives will translate into prohibitive acquisition times; and single-shot acquisitions are most likely to be banned considering the shortened T_1 values, reduced sensitivity, and increased field inhomogeneity (ie, shortened T_2*) one shall expect in small footprint LF magnets.

Yet, approaches exist that have separately tackled some of these limitations. Cartesian and spiral sampling schemes have been used without delay between consecutive time series, resulting in stationary fingerprints.[14,15] The resulting, recurring patterns of signal changes can be repeated indefinitely and used for matching, whereas speed is not sacrificed by long recovery times between acquisitions. Besides, Cartesian acquisition allows for flexible and straightforward image reconstruction.[14,16–19] Optimization strategies have been leveraged to increase the separation between signals with different relaxation properties, with the extra benefit of reducing the total number of images required and, hence, acquisition times.[16–18,20,21] Better discrimination across tissue relaxation properties seems quite potent as MR fingerprints are generally highly correlated regardless of the time series length. Focusing on the latter has allowed drastically reducing the number of required images per time series (down to ≤30), opening up for alternate acquisition strategies such as echo-planar imaging[16–18] while maintaining speed.

Here, we propose OPTIMUM and divert from the original MRF pipeline based on the combination of 3 major changes tailored to LF applications. First, subsampled 3D Cartesian acquisition is performed that allows for straightforward, robust data gridding before image reconstruction. Second, a stationary regime of unique, time-varying, short signal patterns is reached at the steady state for each image voxel. Third, the FA and TR schedule used here was optimized to emphasize signal discrimination at stationary state, across different tissue magnetic properties while bringing robustness to off-resonance and low-SNR conditions.

If promising, a limitation of previously published MRF optimizations lies in the optimization being performed on-resonance, with high SNR. Yet, off-resonance effects can lead to completely different signal patterns that may defeat the optimization performed, even in unbalanced sequences, and a low SNR as encountered at LF could equally jeopardize MRF outcomes. Here, criteria on the amount of transverse magnetization at the steady state were included in our optimization in conjunction with a fully balanced steady state (bSSFP) sequence. Interestingly, MRF originally used bSSFP but quickly departed from it because of off-resonance artifacts. At LF, however, bSSFP provides higher steady-state transverse magnetization (compared with high fields) from reduced T_1 and prolonged T_2 values, making it an imaging sequence of choice.[22] Considering TR $\ll T_1, T_2$, the available signal at steady state is mainly driven by the ratio T_1/T_2 of the imaged sample,[23] which becomes beneficial as static field B_0 goes down.

With OPTIMUM, we could evaluate results at 100 mT (4.25 MHz) in calibrated samples, with T_1/T_2 ranging from 40/15 to 1700/960 milliseconds, and perform quantitative imaging in vivo in the human hand and wrist, providing a set of 6 quantitative maps (T_1, T_2, T_2*, M_0, ΔB_0, and B_1^+). The results presented were obtained from an 8.5-minute, 3-dimensional (3D) scan, in a small footprint dedicated MRI scanner[24] for musculoskeletal applications. To the best of our knowledge, this is the first time that such a set of quantitative maps can be obtained at LF, in 3D, in vivo in human tissue, and with clinically acceptable times.

In the quest for clinical benefits and further medical value, we anticipate that such technique developments may play a critical role in the democratization of LF MRI, from point-of-care, dedicated devices to multipurpose whole body systems.

MATERIALS AND METHODS

OPTIMUM: OPTImized MUltiparametric MRI for Better Tissue Discrimination

Magnetic resonance fingerprinting relies on pattern matching of an acquired NMR signal to a database of simulated signals.[11] The simulated signal showing the highest correlation with the acquired one is identified as the best match, and corresponding NMR properties such as T_1, T_2, off-resonance, and proton density are extracted. Essential to an accurate matching is making sure that, for a given schedule of FAs and TRs, acquired NMR signal trajectories (so called "MR fingerprints") are unique signatures of specific tissue properties. Tissues with different properties that present similar signal evolutions are intrinsically impossible to distinguish, with a risk that MRF will fail. This risk is partially tamed at clinical fields where sufficient SNR may allow distinguishing between correlated signals, but it is particularly exacerbated at LF. Cohen[16,18] showed that signal correlation for a given schedule of FAs and TRs can be evaluated by calculating the dot product matrix H of an optimized dictionary D: $H = D \cdot D$, and optimization schemes were assessed so to diagonalize H for a range of T_1 and T_2 values. Here, OPTIMUM follows a rebooted, similar strategy, accounting for (crucial) off-resonance, converting it to stationary fingerprints, and compromising between discriminatory power and SNR efficiency.

A first pool of n = 10,000 random schedule candidates was generated with MATLAB (MathWorks, Natick, MA) with each 18 FAs/TRs and a fixed echo time (TE) of 9 milliseconds. Echo time was empirically chosen above the minimum achievable (5 milliseconds) to compromise between sufficiently long gradient ramp and plateau times (ie, accounting for hardware limitations), good discriminatory power, and reasonable acquisition times. The explored range for TR was 15 to 40 milliseconds in steps of 5 milliseconds, set by our fixed TE and a target acquisition time of less than 10 minutes, and 0 to 180 degrees for FA with steps of 10 degrees. Dictionaries were simulated accounting for 50 consecutive series of 18 TRs to reach a stationary state across a broad range of magnetic properties. For each FA/TR schedule candidate, 4 dot product matrices H were calculated for 10 pairs of T_1/T_2 properties (Table 1) on-resonance and off-resonance, with δf = 0, 10, 25 (1/max TR), and 67(1/min TR) Hz. Including off-resonance is quite essential as the latter plays a dominant role in the alteration of bSSFP-based MRF signals,[12] beyond the effect of T_1 and T_2 relaxation rates and considering that typical magnetic field homogeneity easily reaches hundreds of hertz in clinical setups.

The selection criteria for the best FA/TR schedule were twofold. First, the mean and standard deviation of the stationary fingerprint magnitude signals $|S_{st}(D)|$ over the last 18 TRs were computed in each simulated dictionary, namely, $\overline{|S_{st}(D)|}$ and σ. On a scale from 0 to 1 (1 being 100% of net magnetization M_0), we noticed that $\overline{|S_{st}(D)|}$ can be rather low (<0.01) in our conditions. Here, only dictionaries with both $\overline{|S_{st}(D)|} \geq 0.05$ and $\sigma \leq 0.05$ were retained to promote a minimum SNR across all simulated signals. In the pool of selected dictionaries, entries in H below a correlation threshold of 0.7 (0 = noncorrelated, 1 = fully correlated) were counted, and the schedule resulting in the largest number of entries was kept. After this initial selection, the FAs in the best schedule candidate were individually challenged in an

TABLE 1. Set of T_1/T_2 Pairs Used in the Described Optimization for OPTIMUM

T_1, ms	45	88	130	190	220	280	330	380	450	500
T_2, ms	19	39	55	83	100	130	150	170	200	230

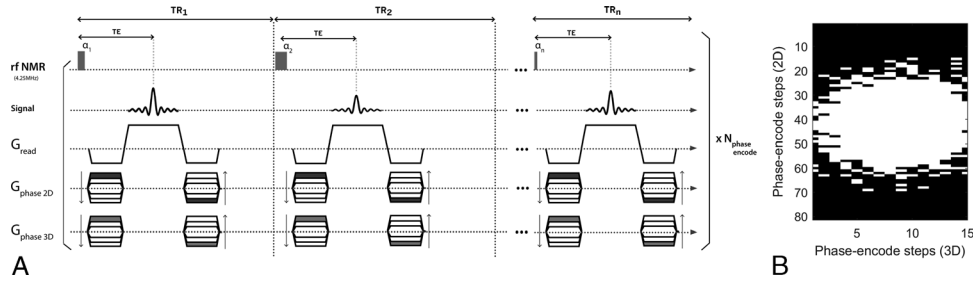

FIGURE 1. OPTIMUM pulse sequence diagram and undersampling pattern used for imaging. A, The acquisition scheme relies on a balanced steady-state approach with Cartesian sampling of *k*-space operating in a sequential fashion. B, A 50% sampling scheme was applied following a Gaussian probability density function.

ordered, iterative manner, by adding or subtracting 10 degrees. For each iteration, a new correlation matrix H was computed. If better (both on SNR and discriminatory aspects), the modification was kept and the FA was further incremented/decremented, or else discarded moving to the next FA in the list. The process was continuously repeated over the entire list of FA until no further improvement was observed. The same iterative approach on TR consistently resulted in prolonged values and hence was not used to maintain reasonably short acquisition times.

The discriminatory performance of the selected OPTIMUM schedule was then compared with simulated schedules from the original MRF approach, also based on bSSFP. For each approach, an array of dot product matrices H was computed with $\delta f = -100{:}0.1{:}100$ Hz, using the magnetic properties described in Table 1. For each set of magnetic properties, the mean and standard deviation on the calculated correlation coefficients was obtained, aiming at diagonalizing H while maintaining low standard deviation scores.

LF OPTIMUM Acquisitions

The OPTIMUM sequence used here is described in Figure 1A, using a Cartesian acquisition and a schedule of n = 18 TRs/FAs. Each *k*-space line was sequentially acquired over the 18 FAs/TRs before moving to the next without pause. The latter strategy ensures that, for each phase encode step, *k*-space lines are rigorously acquired with the same timing (ie, same TE/TR) and prevent potential filtering effects of *k*-space that may arise in single-shot strategies. A generic acquisition strategy was used for both phantom and in vivo measurements, with parameters as follows: sampling rate of 50% following a Gaussian probability density function (Fig. 1B), matrix size 90 × 81 × 15, voxel size [1.5 × 1.5 × 6.5] mm^3 and corresponding field of view [135 × 122.5 × 98] mm^3, bandwidth = 15,000 Hz, number of averages = 2, for a total acquisition time of ~8.5 minutes. Nonsampled *k*-lines in all acquisitions were zero-filled. At 0.1 T, hence more than 15 times lower field strength than the original MRF work (ie, $\sim 15^{3/2}$ lower sensitivity[1]), with no magnetic nor radiofrequency shielding, the optimized 18 FA/TR schedule used here brings the acquisition of a single 2D partition to 34 seconds, compared with 12 seconds in the original MRF study.

LF MRI System

All experiments were performed on a small footprint, biplanar 0.1 T MRI scanner[24] (Fig. 2A), in combination with a 60 × 120–mm^2 inside diameter, 120-mm-long transmit/receive solenoid coil (Fig. 2B), capacitively tuned and inductively matched at F_0 = 4.256 MHz. The MRI scanner features a transverse, horizontal static magnetic field B_0 and a 17-cm bore. The 0.1 T resistive magnet (EAR54L, Drusch & Cie, Rueil-Malmaison, France) is water cooled and powered by a separated power unit including the magnet main power supply and the gradient power amplifiers. The scanner is equipped with a set of 3 biplanar gradients (x, y, z) which can presently achieve a calibrated maximum gradient strength of 10 mT/m. The console used to drive the MRI hardware and for signal collection is a Cameleon3 (RS2D, Strasbourg, France) respectively equipped with 2 radiofrequency transmit and 4 receive channels. Radiofrequency transmit operations were performed via a 500 W pulsed amplifier (BT00500-ALphaS, Tomco Technologies, Stepney, Australia) connected to the coil via a passive transcoupler (NMR Service GmbH, Erfurt, Germany). For receive operations, the used transmit/

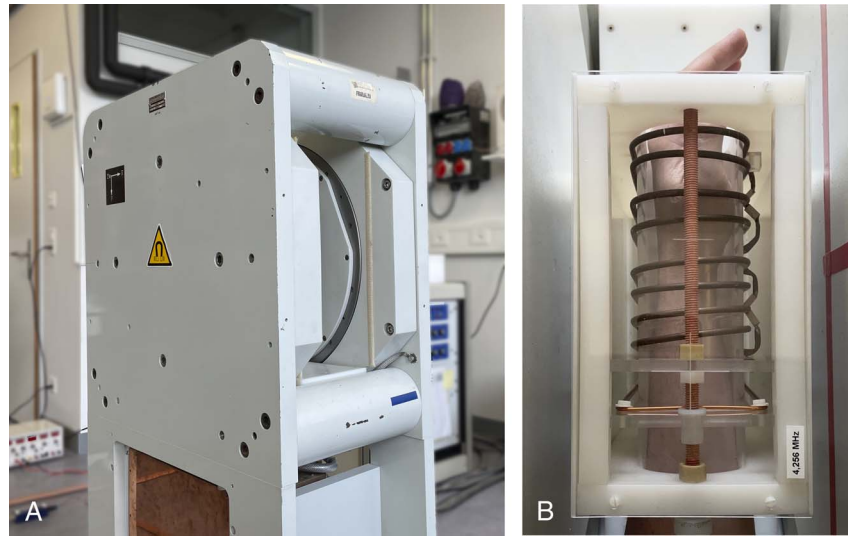

FIGURE 2. Experimental setup. View of (A) the small footprint, biplanar 0.1 T scanner and (B) the transmit/receive solenoid coil used.

TABLE 2. Sets of Parameters Used in the Spectroscopic Experiments to Quantify T_1 and T_2

	Inversion Recovery (T_1)		CPMG (T_2)	
Sol. ID	**Inversion Time (ms)**	**No. Steps**	**TE, δTE (ms)**	**ETL**
1	10	101	5	76
2	10	101	5	101
3	20	101	5	201
4	40	71	5	301
5	45	71	5	401
6	60	71	5	401
7	60	71	5	401
8	60	71	5	401
9	150	51	5	601
10	200	51	5	601
11	200	51	5	601
12	200	51	5	1001

The CPMG sequence used had TE = δTE = 5 milliseconds, and variable ETLs. ETL indicates echo train length; TE, echo time.

receive solenoid coil (Fig. 2B) was connected to a custom low-noise preamplifier developed in-house.[25]

Dictionary Design

As we are using a fully balanced MR acquisition strategy, our computed dictionary relies on the Bloch formalism as described by Ma et al.[11] Dictionaries were simulated using Matlab with 4 dimensions: T_1, T_2, ΔB_0, and FA homogeneity (B_1^+) as a scaling factor of the desired, nominal FAs. For matching, T_1 ranged from 5 to 1900 milliseconds (in increments of 5 milliseconds from 5 to 150 milliseconds, in increments of 10 milliseconds from 160 to 400 milliseconds, in increments of 25 milliseconds from 425 to 1000 milliseconds, and in increments of 50 milliseconds from 1050 to 1900 milliseconds). T_2 in the simulated dictionary ranges from 4 to 1000 milliseconds (in increments of 2 milliseconds from 4 to 60 milliseconds, in increments of 5 milliseconds from 65 to 200 milliseconds, in increments of 10 milliseconds from 220 to 500 milliseconds, and in increments of 25 milliseconds from 525 to 1000 milliseconds). Static magnetic field ΔB_0 variations are included as off-resonance frequencies ranging between ±80 Hz in steps of 1 Hz. Flip angle homogeneity ranges from 65% to 125% of nominal FAs with increments of 5%. Data matching to recover OPTIMUM maps from a ~8 M entries dictionary required ~1.5 minutes on a desktop computer equipped with a 2176 core/8 GB DDR6 memory GPU engine (GEFORCE RTX 2060 Super, NVIDIA, Santa Clara, CA). Getting both T_2 and off-resonance maps from the MRF pipeline, we could infer a voxel wise estimation of T_2* and hence add a sixth quantified map to the MRF reconstructed set following $\frac{1}{T_2^*} = \frac{1}{T_2} + \frac{1}{T_2'}$ and assuming $\frac{1}{T_2'} = \frac{\gamma}{2\pi} \times \Delta B_0$.

Validation in Phantoms

OPTIMUM at 0.1 T was validated in 2 calibrated, 6-bottle phantoms made of borosilicate glass with Teflon caps (30 mL, ∅2 cm ID) containing $MnCl_2$ in deionized water at different concentrations. For each solution, T_1 and T_2 relaxation rates were respectively measured from gold standard inversion recovery and echo-train-based (CPMG) spectroscopic experiments (parameters in Table 2), with probed relaxation rates ranging from T_1/T_2 = 43/19 milliseconds to 1700/960 milliseconds (Table 3). Static magnetic field homogeneity B_0, T_2*, and B_1^+ obtained with OPTIMUM were compared with ground truth experiments in one of the calibrated 6-bottle phantoms. A 3D gradient echo sequence with varying TEs (TE, 6:5:31 milliseconds; TR, 40 milliseconds) and the same geometry was performed that allowed to fit T_2* voxelwise. The first 2 echoes of the latter imaging sequence were used to infer a reference B_0 map. A dual flip-angle (90°/45°), 3D gradient echo approach using the same geometry was used to obtain a reference B_1^+ map, with parameters of TE of 6 milliseconds and TR of 1.6 seconds (ie, ~5 times the expected longer T_1 in the investigated calibrated phantom). OPTIMUM robustness to off-resonance was challenged by performing experiments in different off-resonance conditions. Respectively, OPTIMUM was performed at 13 and 35 Hz off-resonance that can be achieved by manually varying the magnetic field of the resistive 0.1 T scanner, and ultimately at 35 Hz off-resonance with an altered shim.

Multiparametric Imaging In Vivo

OPTIMUM was performed in vivo in the human hand and wrist. Axial images were acquired in 3D in 8.5 minutes with parameters identical to the phantom measurements. A total of 6 quantified maps could be inferred (M_0, T_1, T_2, T_2*, ΔB_0 and B_1). Signal trajectories were compared across different tissue types (eg, bone marrow, bone, tendon, and muscle).

RESULTS

OPTIMUM

When we compare the discriminatory power of our optimized schedule against the original MRF types of pseudo-random schedules (type 1 and 2) described by Ma et al[11] (Fig. 3), it seems that all schedules perform reasonably well on resonance (ΔB_0= 0 Hz) for our set of

TABLE 3. OPTIMUM Accuracy in a Calibrated Phantom

Sol. ID	[$MnCl_2$] (mM)	T_1 (ms)	T_1 OPTIMUM (ms)	T_2 (ms)	T_2 OPTIMUM (ms)
1	1.35	43 ± 0.7	43.9 ± 3	19 ± 0.3	15.5 ± 1.5
2	0.65	89 ± 1	85.5 ± 7	39 ± 1	28.5 ± 2
3	0.45	127 ± 2	125.6 ± 8	57 ± 0.2	38.5 ± 3
4	0.3	185 ± 4	194.8 ± 13	83 ± 0.5	53 ± 5
5	0.25	221 ± 5	241 ± 13	101 ± 0.2	66 ± 5
6	0.16	333 ± 6	354 ± 27	152 ± 0.3	94 ± 6
7	0.14	378 ± 8	313 ± 48	170 ± 0.3	77 ± 13
8	0.10	496 ± 9	503 ± 55	231 ± 1	146 ± 31
9	0.07	664 ± 13	709 ± 110	315 ± 1	176 ± 30
10	0.055	807 ± 17	982 ± 148	384 ± 1	261 ± 51
11	0.04	1016 ± 29	1083 ± 228	492 ± 1.5	365 ± 66
12	0.015	1723 ± 25	433 ± 296	960 ± 1.5	259 ± 158

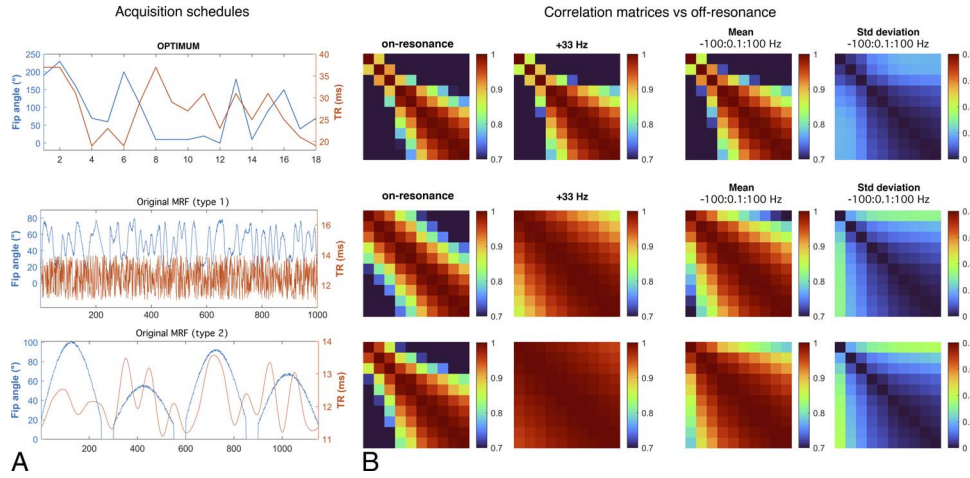

FIGURE 3. Acquisition schedules and correlation matrices *H* computed as a function of off-resonance. Top row: OPTIMUM with 18 FAs/TRs exhibits good discriminatory power (diagonalized *H*) across a broad range of off-resonance frequencies, with maintained low standard deviation. Central to bottom row: original MRF schedules with ≥1000 FAs/TRs exhibit reasonable discriminatory power on-resonance, and lower overall performance off-resonance. Correlation matrices were all calculated with the same 10 pairs of T_1/T_2 properties (Table 1).

T_1/T_2 values (Table 1), with sensibly better performance for OPTIMUM. Type 1 and 2 MRF schedules exhibit a mean correlation of 0.85 ± 0.16 and 0.83 ± 0.19, respectively, whereas OPTIMUM provides 0.67 ± 0.33. Off-resonance, however, both type 1 and 2 schedules show reduced discriminatory power, even for species an order of magnitude apart, when OPTIMUM maintains similar performance. This can be seen for a given frequency offset (here 33 Hz, randomly picked) and similarly over an averaged correlation matrix across 2000 frequency offsets (−100:0.1:100 Hz). At 33 Hz off-resonance, type 1 and 2 MRF schedules show a mean correlation of 0.97 ± 0.035 and 0.99 ± 0.012, respectively, whereas OPTIMUM exhibits 0.71 ± 0.31. Over the averaged 2000 frequency offsets, type 1 and type 2 MRF schedules show a mean correlation of 0.93 ± 0.082 and 0.95 ± 0.057, respectively, whereas OPTIMUM exhibits 0.73 ± 0.31. The latter trend is further confirmed by the corresponding standard deviations, showing high discrepancies (>0.4) in type 1 and 2 schedules versus a maintained low value with OPTIMUM (<0.2). We observe nonetheless that both optimized and pseudo-random acquisition strategies lack discriminatory power for T_1/T_2 greater than 330/150 milliseconds, even at resonance.

Validation in Calibrated Phantoms

Over the investigated broad range of relaxation rates, LF OPTIMUM seems to be in rather good agreement with gold standard experiments for 11 of 12 samples tested (Fig. 4), with comparable T_1 values retrieved ($y_{T1} = 1.092 \cdot x_{T1}$) and a tendency to underestimate T_2 ($y_{T2} = 0.70 \cdot x_{T2}$), in particular at long relaxation rates. We note that the extracted T_1 and T_2 standard deviations for each sample also increases with increased T_1 and T_2, noticeably for T_1/T_2 380/170 milliseconds or greater, as can be equally observed on the corresponding mean T_1 and T_2 maps. For both T_1 and T_2, we notice an outlier value retrieved in the 12th sample tested with the longest T_1/T_2 probed (1700/960 milliseconds), with both highly underestimated retrieved values and the largest standard deviation across the sample. The latter data point was not used in the calculation of linear regressions. Calibrated B_0 and B_1^+ also show good agreement with OPTIMUM (Figs. 5A, B). Subtle discrepancies can be observed with respect to B_0 that originate from slightly different shimming conditions. The calibration 6-echo scan performed to retrieve T_2* was compared with the one inferred with OPTIMUM (Fig. 6), yet using a corrected $T_{2\ \mathrm{corr}} = \frac{T_{2\ \mathrm{optimum}}}{0.7}$ as the latter shows a tendency to be underestimated ($y_{T2} = 0.70 \cdot x_{T2}$). The OPTIMUM inferred T_2* maps are in good agreement with the calibration experiment (Fig. 6A) when confidence in the performed voxel-wise fit is

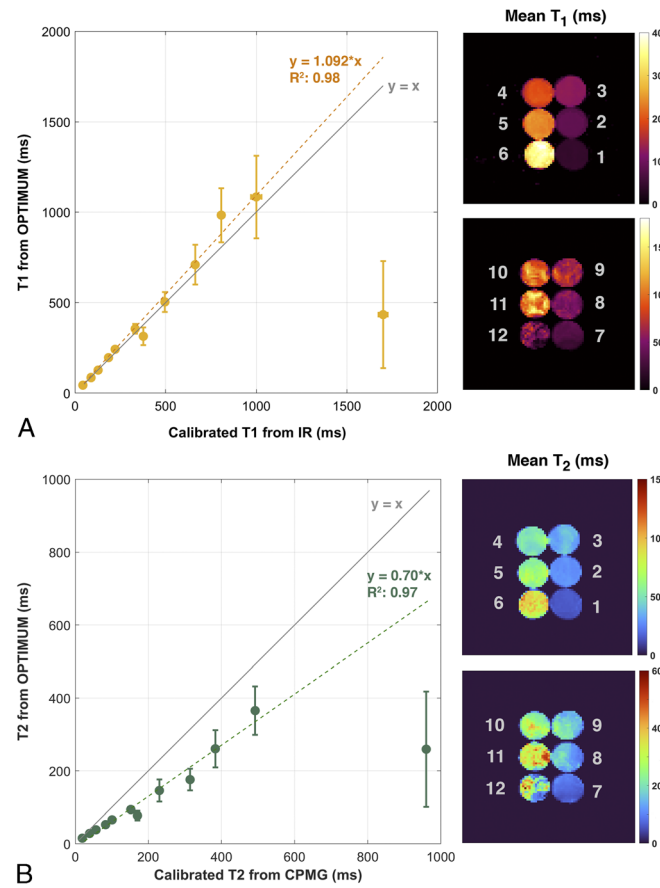

FIGURE 4. Comparison of LF OPTIMUM with gold standard spectroscopic measurements. T_1 (A) and T_2 (B) values retrieved in calibrated phantoms compared with standard inversion-recovery and spin echo techniques, and their corresponding mean relaxation maps over the phantom volumes.

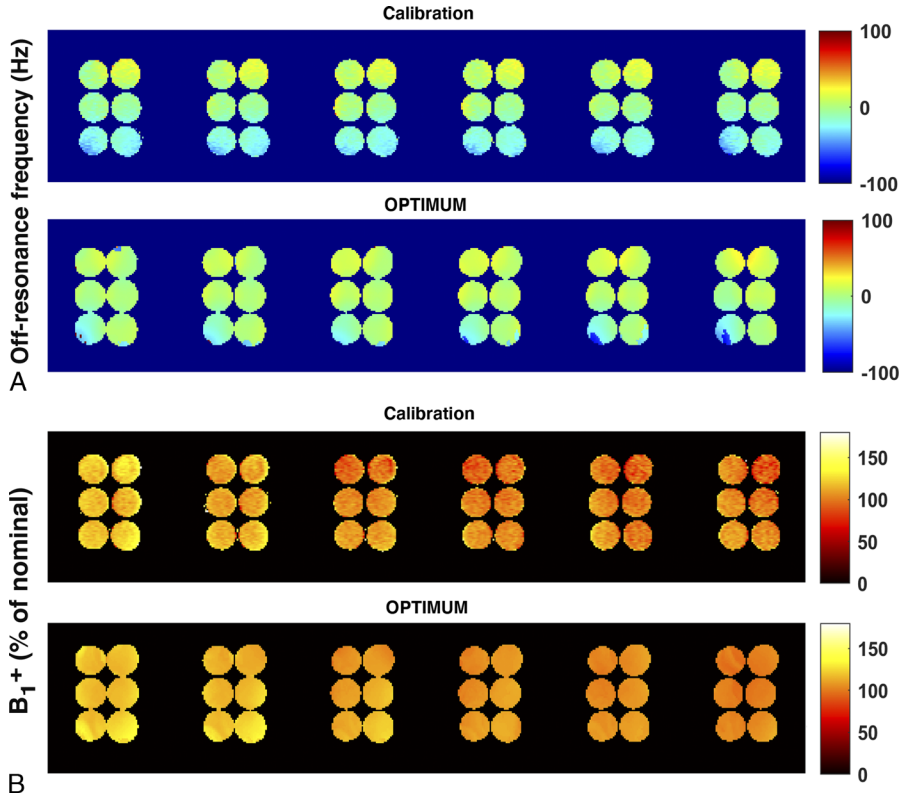

FIGURE 5. Comparison of calibrated static magnetic field and radiofrequency FA homogeneity with OPTIMUM. (A) Off-resonance frequency (in Hz) and (B) B_1^+ (in percentage of nominal FA) displayed for 6 central slices.

good (Fig. 6B). Discrepancies arise, particularly pronounced in sample tubes 4 and 5 (>50%), in areas exhibiting poor fitting performance (ie, low R^2). Robustness to off-resonance is reported in Figure 7. At 35 Hz off-resonance and with an altered shim (Fig. 7A), OPTIMUM can retrieve relaxation parameters in the calibrated phantom while depicting the expected change in static magnetic field. It shows similarly good performance in all the off-resonance scenarios investigated (13 Hz, 35 Hz, and 35 Hz + altered shim conditions) in comparison with the reference on-resonance experiment (Fig. 7B).

Multiparametric Imaging In Vivo

Quantitative maps acquired in the hand and wrist allow successfully distinguishing main anatomical structures (Fig. 8A) and their associated relaxation properties, reported in Table 4. Bones, tendons, and

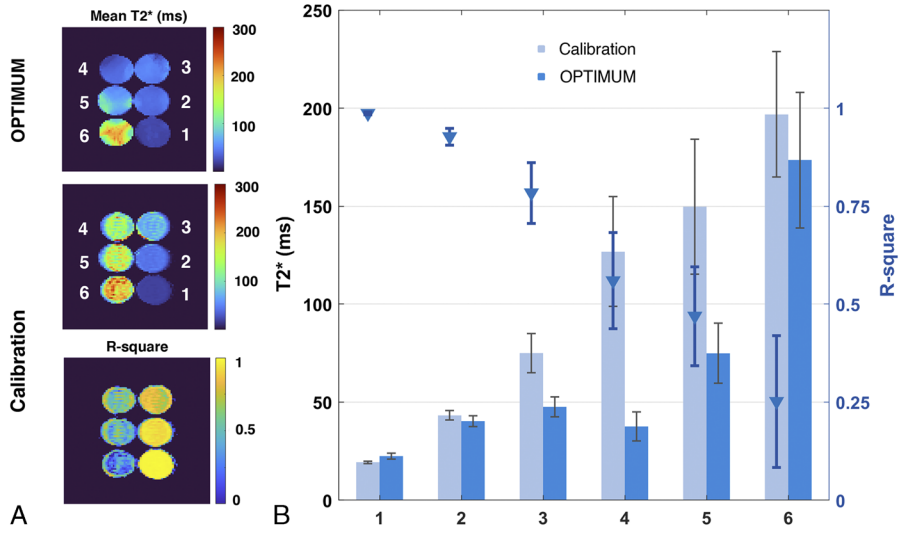

FIGURE 6. Comparison of calibrated T_2* with OPTIMUM. A, Mean T_2* and R-square maps resulting from voxel wise curve fitting vs OPTIMUM. B, Corresponding bar graphs reported for each sample.

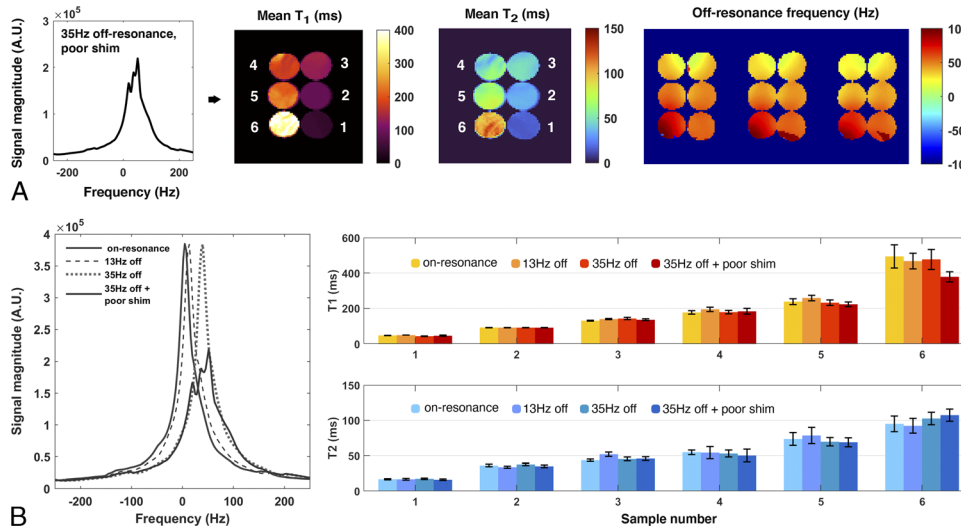

FIGURE 7. Assessment of OPTIMUM robustness to off-resonance. A, Mean T_1, T_2 maps, and off-resonance (3 central slices displayed) in a 35 Hz off-resonance scenario with altered shim. B, Reported mean T_1 and T_2 values in 4 distinct scenarios, respectively, on-resonance, 13 Hz and 35 Hz off-resonance, and 35 Hz off-resonance in combination with an altered shim.

large blood vessels, as well muscle, skin, and fatty tissue, can be observed. Magnetic field inhomogeneity reaches a maximum of ±80 Hz across the limb, equivalent to 19 ppm at 4.256 MHz (100 mT). The extracted B_1^+ maps reflect accurately the expected profile from the coil used, with higher FAs closer to the coil wire, at the periphery of the imaged object. Tissue species such as bone marrow and muscle exhibit very different signal evolutions (Fig. 8B), whereas tendon seems rather close to bone. With T_1/T_2~1, bone marrow exhibits the highest and most recurring signal on the OPTIMUM time series recorded (Fig. 8C), which is expected from the bSSFP nature of the sequence.

DISCUSSION

Relying on both a high duty cycle for data acquisition and favorable, reduced T_1/T_2 ratios at lower magnetic fields, bSSFP running under the hood of OPTIMUM is a very efficient way to rationalize SNR

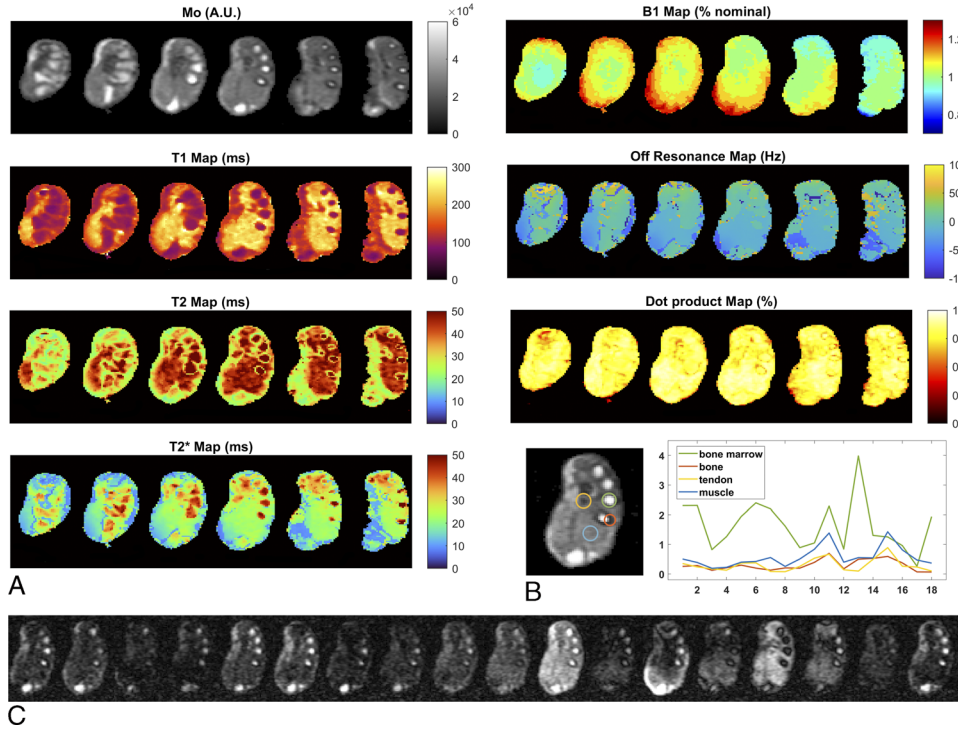

FIGURE 8. LF OPTIMUM results in vivo at 0.1 T. A, Quantified maps in the human hand/wrist that includes proton density M_0, T_1, T_2, T_2*, B_0, FA homogeneity B_1^+, and matching efficiency (dot product map) for 6 central slices. Matrix size is 90 × 81 × 15, corresponding voxel size is [1.5 × 1.5 × 6.5] mm^3. Total imaging time is 8.5 minutes with number of averages = 2. B, Signal evolution (ie, MR fingerprints) reported for different tissue types in a central slice. (C) Corresponding MR image series.

TABLE 4. Compilation of T_1, T_2, and T_2* With OPTIMUM for a Selection of Tissue Types

Tissue Type	T_1 (ms)	T_2 (ms)	T_1/T_2	T_2* (ms)
Muscle	237 ± 16	48 ± 4	5	22.5 ± 0.8
Tendon	202 ± 22	41 ± 4	5	24 ± 1.6
Bone	171 ± 4	39 ± 3	4.4	26 ± 5
Bone marrow	98 ± 6	69 ± 6	1.4	49 ± 3
Fat layer	131 ± 14	30 ± 5	4.4	25 ± 5

per unit time. bSSFP alone can bring high SNR but limited contrast, and a high sensitivity to off-resonance artifacts. Here, off-resonance can be used as a discriminatory feature for matching purposes, and the high SNR/unit time is key to acceptable acquisition times.

The optimization performed and subsequent reduction of the acquisition schedule were aimed to bring good discriminatory performance across a range of relaxation rates relevant to LF MRI (Table 1). The latter allows porting the MRF framework to straightforward Cartesian acquisitions, without heavily impacting acquisition times. With no particular calibration nor preliminary processing, the acquired, undersampled raw data are then zero-filled before a 3D Fourier transform is applied (Fig. 8C), hence providing a robust and straightforward reconstruction pipeline before matching to a precomputed dictionary. Simulations show that OPTIMUM maintains good discriminatory power across the investigated range of relaxation rates (Fig. 3B), both on- and off-resonance, whereas regular MRF approaches tend to generally worsen off-resonance. Robustness to off-resonance is further confirmed in experiments (Fig. 7), where both magnetic properties and static magnetic field maps can be accurately retrieved, even in altered shim conditions. The length of the acquisition schedule, as a result, should not be seen as a validity criterion to obtain good signal discrimination.

We hypothesize that optimization is critical to LF regimes where the combination of low SNR and highly correlated signals may simply defeat the technique. However, as regular MRF seems to perform well at clinical fields, it would be interesting to rigorously assess the impact of such an optimization, whether it is beneficial to discriminate better across species or if the inherently higher SNR allows to navigate through signal similarities. To that end, optimizations could be performed over both short and large trajectories, for stationary or transient state approaches, and compared with nonoptimized MRF for different SNR regimes. Scaling-up at larger FA/TR schedules may require larger computational time, or further compartmenting of computational tasks to be effective, yet that shall not hinder generic MRF applications, being only a 1-time operation.

OPTIMUM validation in calibrated phantoms demonstrates the expected linear relationship between manganese chloride concentration and the retrieved T_1 and T_2 relaxation rates, at the exception of 1 outlier data point (T_1/T_2 = 1700/960 milliseconds). With reasonably good T_1 estimates (Fig. 4A), we tend to consistently underestimate T_2 (Fig. 4B). A plausible cause to such underestimation could be intravoxel phase dispersion, as demonstrated by Chiu et al,[26] that needs to be further investigated. The type of optimization, the range of sequence parameters (FA, TR), the set of relaxation rates, and further, the dictionary used for the matching may also be in cause. In the meantime, one could imagine to simply correct T_2 maps in postprocessing for more realistic estimates (at least in phantom experiments), so long that the observed trend proves stable. After such correction, we notice that T_2* maps from OPTIMUM are in reasonably good agreement with T_2* maps generated from a multiecho, calibration sequence (Fig. 6). Discrepancies can, however, arise when curve-fitting exhibits poor performance. The latter highlights the difficulty in performing and trusting a single calibration scan with a broad range of relaxation parameters (here, from T_1/T_2 = 43/19 milliseconds to 333/152 milliseconds). Instead, several calibration scans would be needed that would inevitably impact the overall experiment time.

Overall, OPTIMUM shows larger standard deviations with increasing relaxation rates (Fig. 4), noticeably in sample 7 to 12 (deviations >15%), both in the plots and corresponding maps displayed. An explanation could be the low discriminatory performance of OPTIMUM when T_1/T_2 goes from 330/150 milliseconds to 500/230 milliseconds (Fig. 3B), with corresponding mean correlation scoring very high, from 96% to 99.5%. It is also possible that too many banding artifacts arise, impeding SNR and hence preventing good matching performance.[12] Alternatively, the simulated dictionaries could be enriched with a higher density of parameters or with additional parameters for higher accuracy. In the latter case, innovative approaches[27–30] will then be needed to keep the reconstruction time low, bringing options to rationalize acquired datasets over longer time periods. Overall, it is quite reasonable, however, that the observed performance drop occurs where the optimization performs the least, and future work on the optimization at longer relaxation times should beneficially improve performance.

In vivo, we successfully report on fast quantitative imaging in the human hand and wrist at 0.1 T, providing a total of 6 quantified metrics in 3D. Major anatomical structures can be resolved, and their corresponding relaxation rates mapped. Comparison with T_1 and T_2 relaxometry in vivo in humans is not trivial as the literature is scarce, but OPTIMUM shows quantified values in the skeletal muscle and fat in reasonably good agreement with previous work in animal and humans (generally only T_1 is available) that compiles living and postmortem measurements.[31–33]

CONCLUSION

Largely unexplored in vivo, relaxation dynamics are increasingly influenced by molecular interactions at lower fields and present inherently larger dispersion that could result in unique contrasts.[19,34] As the interest in LF MRI research resurfaces, time-efficient quantification of magnetic properties in tissue will become more and more essential to address fundamental questions on the diagnosis potential of lower field strengths. Relying on the grounds of MRF, OPTIMUM brings an added, tailored layer to LF MRI. From the optimized, enhanced discrimination across NMR signals within a broad range of static field inhomogeneities, it allows navigating in low-SNR regimes. From its reduced amount of temporal steps, it allows mitigating total acquisition times while giving the choice to use Cartesian (privileged here for robustness) or non-Cartesian acquisition schemes. As such, OPTIMUM is currently the only technique capable to characterize simultaneously M_0, T_1, T_2, T_2*, B_0, and B_1^+ in 3D, with acquisition times acceptable for clinical routine. Leveraging SNR efficient sequences and transferring the complexity associated with quantitative MR in silico, OPTIMUM is compelling with simpler and scalable technologies that could shape the future of mobile diagnostics in radiology. It could be central to the contemporary investigation of novel contrasts, from markers of ischemic/hemorrhagic stroke in the intensive care unit, of inflammation in MSK applications, to subtle underlying changes for the screening or staging of cancer.

ACKNOWLEDGMENTS

The author would like to warmly acknowledge Najat Salameh for her scientific input, advices and fruitful discussions while crafting the manuscript and Maksym Yushchenko for his support in converting the OPTIMUM sequence into the laboratory programming environment.

REFERENCES

1. Sarracanie M, Salameh N. Low-field MRI: how low can we go? A fresh view on an old debate. *Front Phys*. 2020;8:172.

2. Marques JP, Simonis FFJ, Webb AG. Low-field MRI: An MR physics perspective. *J Magn Reson Imaging*. 2019;49:1528–1542.
3. Wald LL, McDaniel PC, Witzel T, et al. Low-cost and portable MRI. *J Magn Reson Imaging*. 2020;52:686–696.
4. Salameh N, Sarracanie M. Re-envisioning low-field MRI. *MAGNETOM Flash*. 2020;1:8–13.
5. Runge VM, Heverhagen JT. Advocating the development of next-generation, advanced-design low-field magnetic resonance systems. *Invest Radiol*. 2020;55: 747–753.
6. Fischer HW, Rinck PA, van Haverbeke Y, et al. Nuclear relaxation of human brain gray and white matter: analysis of field dependence and implications for MRI. *Magn Reson Med*. 1990;16:317–334.
7. Deoni SCL, Rutt BK, Peters TM. Rapid combined T1 and T2 mapping using gradient recalled acquisition in the steady state. *Magn Reson Med*. 2003;49:515–526.
8. Heule R, Ganter C, Bieri O. Triple echo steady-state (TESS) relaxometry. *Magn Reson Med*. 2013;71:230–237.
9. Nguyen D, Bieri O. Motion-insensitive rapid configuration relaxometry. *Magn Reson Med*. 2016;78:518–526.
10. Metere R, Kober T, Möller HE, et al. Simultaneous quantitative MRI mapping of T1, T2* and magnetic susceptibility with multi-echo MP2RAGE. *PLoS One*. 2017;12:e0169265.
11. Ma D, Gulani V, Seiberlich N, et al. Magnetic resonance fingerprinting. *Nature*. 2013;495:187–192.
12. Jiang Y, Ma D, Seiberlich N, et al. MR fingerprinting using fast imaging with steady state precession (FISP) with spiral readout. *Magn Reson Med*. 2015;74: 1621–1631.
13. Cao X, Liao C, Wang Z, et al. Robust sliding-window reconstruction for accelerating the acquisition of MR fingerprinting. *Magn Reson Med*. 2016;495:187–110.
14. Amthor T, Doneva M, Koken P, et al. Magnetic resonance fingerprinting with short relaxation intervals. *Magn Reson Imaging*. 2017;41:22–28.
15. Guenthner C, Kozerke S, Sarracanie M. Fast multiparametric imaging in the brain using a stationary balanced steady state Cartesian approach. In: *27th Annual Meeting of the International Society for Magnetic Resonance in Medicine and Biology*. Montreal, Canada; 2019: Abstract 4408.
16. Cohen O, Rosen MS. Algorithm comparison for schedule optimization in MR fingerprinting. *Magn Reson Imaging*. 2017;41:15–21.
17. Sarracanie M, Cohen O, Rosen MS. 3D balanced-EPI magnetic resonance fingerprinting at 6.5 mT. In: *23rd Annual Meeting of the International Society for Magnetic Resonance in Medicine and Biology*. Toronto, Canada; 2015: Abstract 3385.
18. Cohen O, Sarracanie M, Rosen MS, et al. In Vivo Optimized Fast MR Fingerprinting in the Human Brain. In: *24th Annual Meeting of the International Society for Magnetic Resonance in Medicine and Biology*. Singapore; 2016: Abstract 0430.
19. Sarracanie M, Herisson F, Salameh N, et al. A marker for hyperacute stroke at ultra-low magnetic field. In: *24th Annual Meeting of the International Society for Magnetic Resonance in Medicine and Biology*. Singapore; 2016: Abstract 1440.
20. Zhao B, Haldar JP, Liao C, et al. Optimal experiment design for magnetic resonance fingerprinting: Cramér-Rao bound meets spin dynamics. *IEEE Trans Med Imaging*. 2019;38:844–861.
21. Kara D, Fan M, Hamilton J, et al. Parameter map error due to normal noise and aliasing artifacts in MR fingerprinting. *Magn Reson Med*. 2019;81:3108–3123.
22. Sarracanie M, LaPierre CD, Salameh N, et al. Low-cost high-performance MRI. *Sci Rep*. 2015;5:15177.
23. Scheffler K, Lehnhardt S. Principles and applications of balanced SSFP techniques. *Eur Radiol*. 2003;13:2409–2418.
24. Constantinesco A, Choquet P, Cauffet G, et al. Low-field dedicated and desktop magnetic resonance imaging systems for agricultural and food applications. *Magn Reson Chem*. 1997;35:S69–S75.
25. Quirin T, Yushchenko M, Salameh N, et al. High-input impedance preamplifiers for multi-channel strategies at low frequency. In: *Annual meeting of the European Society for Magnetic Resonance in Medicine and Biology*. 2020: Abstract L01.108.
26. Chiu S-C, Lin T-M, Lin J-M, et al. Effects of RF pulse profile and intra-voxel phase dispersion on MR fingerprinting with balanced SSFP readout. *Magn Reson Imaging*. 2017;41:80–86.
27. McGivney DF, Pierre E, Ma D, et al. SVD compression for magnetic resonance fingerprinting in the time domain. *IEEE Trans Med Imaging*. 2014; 33:2311–2322.
28. Cauley SF, Setsompop K, Ma D, et al. Fast group matching for MR fingerprinting reconstruction. *Magn Reson Med*. 2015;74:523–528.
29. Cohen O, Zhu B, Rosen MS. MR fingerprinting Deep RecOnstruction NEtwork (DRONE). *Magn Reson Med*. 2018;80:885–894.
30. Yu N, Kim JY, Han D, et al. Three-dimensional magnetic resonance fingerprinting in neonates: quantifying regional difference and maturation in the brain [published online ahead of print June 8, 2021]. *Invest Radiol*.
31. Bottomley PA, Foster TH, Argersinger RE, et al. A review of normal tissue hydrogen NMR relaxation times and relaxation mechanisms from 1-100 MHz: dependence on tissue type, NMR frequency, temperature, species, excision, and age. *Med Phys*. 1984;11:425–448.
32. Alanen AM, Parkkola RK, Lillsunde IGV, et al. The effects of the method of death and lapsed time on proton relaxation time T1 in autopsied muscle samples. *Invest Radiol*. 1993;28:529–532.
33. Markkola AT, Aronen HJ, Ramadan UA, et al. Determination of T1ρ values for head and neck tissues at 0.1 T: a comparison to T1 and T2 relaxation times. *Magn Reson Imaging*. 1998;16:377–383.
34. Broche LM, Ross PJ, Davies GR, et al. A whole-body fast Field-cycling scanner for clinical molecular imaging studies. *Sci Rep*. 2019;9:10402.